A Bayesian theoretic approach to multi-scale complex phase order representations

Alexander Wong, *Member, IEEE*

Abstract—This paper explores a Bayesian theoretic approach to constructing multi-scale complex phase order representations. We formulate the construction of complex phase order representations at different structural scales based on scale space theory. Linear and nonlinear deterministic approaches are explored, and a Bayesian theoretic approach is introduced for constructing representations in such a way that strong structure localization and noise resilience is achieved. Experiments illustrate its potential for constructing robust multi-scale complex phase order representations with well-localized structures across all scales under high noise situations. Illustrative examples of applications of the proposed approach is presented in the form of multimodal image registration and feature extraction.

Index Terms—Bayesian, complex phase order, registration, feature extraction

I. INTRODUCTION

A powerful approach for structural analysis of visual data that has garnered attention in the research community is the concept of local phase, which has been shown to provide important structural information about a scene [1], [2], [3]. A particularly interesting tool based on the concept of local phase for extracting structural information from visual data is the idea of complex phase order [1], [2], [4], whose motivation stems from the theory that the degree of order amongst local phase across multiple complex scales has a strong correspondence to perceptual structural significance within visual data. This theory is reinforced by physiological evidence showing that the human vision system show strong response to visual data with high complex phase order [2]. Besides the biological ties to the human vision system, complex phase order allows for the capturing of structural characteristics of visual data largely independent of intensity, making it well suited for constructing illumination invariant structural representations of the visual data. Given these benefits, complex phase order has become used in a number of different image processing and computer vision applications such as image focus assessment [5], [6], face recognition [7], [8], segmentation [9], [10], [11], and registration [12].

In particular, the problem of multimodal image registration is an important problem to tackle using complex phase order, as it has been shown to be a valuable tool in medical image processing given the variety of medical applications ranging from computer-assisted surgery [13] to clinical disease analysis [14], [15]. Multimodal image registration has become particularly important in the medical community given the rise in multimodal disease analysis, where imaging data acquired using different medical imaging modalities (e.g., magnetic resonance (MRI), computed tomography (CT), and ultrasound) provide different anatomical and functional information about the human body that can, when combined, significantly improve the detection of various diseases such as cancer [15], [16]. Some of the main challenges when dealing with multi-modal image registration include intensity mapping differences due to differing image modalities, illumination and contrast inhomogeneities, and the presence of noise. Many of these issues remain important challenges in the development of multimodal image registration methods, particularly the issue of noise.

Despite the usefulness of complex phase order as a powerful tool in computer vision applications, there are some inherent limitations that calls for further study and exploration on the topic. First, complex phase order represents all structural information within the visual data together as a single entity, making the separation and analysis of differently scaled structural characteristics difficult to achieve. For example, in the application of skin lesion segmentation, it is very useful to separate unwanted fine scale structures such as body hair from the large scale structures such as lesions to improve lesion segmentation accuracy. Second, despite advances made to reduce noise sensitivity [4], [12], the computation of complex phase order continues to suffer significant degradation under high noise scenarios.

In this study we propose a novel multi-scale approach to constructing complex phase order representations. We formulate the construction of complex phase order representations at different structural scales using scale space theory. We then introduce a novel approach for obtaining representations using a Bayesian theoretic framework that provide strong structure localization and noise resilience. Such a multi-scale extension of complex phase order representations is of great interest given the potential for facilitating robustness in a variety of computer vision tasks.

The paper is organized as follows. An overview on complex phase order is described in Section II. The concept of multi-scale complex phase order representations is described in Section III. A Bayesian theoretic approach to constructing multi-scale complex phase order representations is described in Section V. Experimental results comparing the different multi-scale complex phase order representations is presented in Section VI. An illustrative example of the Bayesian theoretic approach being applied to multimodal image registration is presented in Section VII. Finally, an illustrative example of the Bayesian theoretic approach being applied to feature extraction is presented in Section VIII.

Alexander Wong is with U. of Waterloo, Waterloo, Canada N2L 3G1. a28wong@uwaterloo.ca

II. COMPLEX PHASE ORDER

Let $f = f(\underline{x})$ denote the visual data. For each pixel in f, we wish to compute the complex phase $\phi_{s,\theta}(\underline{x})$ at each scale s and orientation θ. To achieve this, we first construct a multi-scale complex wavelet representation of f, denoted as F, using a complex wavelet transform such as the dual-tree complex wavelet transform [17] and Log-Gabor complex wavelet transform [18], consisting of α scales and β orientations. In our implementation, the over-complete, un-decimated Log-Gabor complex wavelet transform proposed by Fischer et al. [18] was performed on f over $\beta = 6$ orientations (0°, 30°, 60°, 90°, 120°, and 150°) and $\alpha = 4$ scales (wavelengths of 3,9,27, and 81 pixels were used to maintain a two octave bandwidth), although the dual-tree complex wavelet transform may also be used.

After the complex wavelet transform, each point $\underline{x}$ in F is represented by a set of $\alpha\beta$ complex wavelet responses $\Upsilon_{s,\theta}(\underline{x})$, which can be expressed by

$$\Upsilon_{s,\theta}(\underline{x}) = A_{s,\theta}(\underline{x}) \exp\left[j\phi_{s,\theta}(\underline{x})\right], \quad (1)$$

where $A_{s,\theta}(\underline{x})$ and $\phi_{s,\theta}(\underline{x})$ are the complex amplitude and phase, respectively, and can be expressed by

$$A_{s,\theta}(\underline{x}) = \sqrt{\left(f(\underline{x}) * J_{s,\theta}^e\right)^2 + \left(f(\underline{x}) * J_{s,\theta}^o\right)^2}, \quad (2)$$

and,

$$\phi_{s,\theta}(\underline{x}) = \tan^{-1}\left(\frac{f(\underline{x}) * J_{s,\theta}^e}{f(\underline{x}) * J_{s,\theta}^o}\right), \quad (3)$$

where $J_{s,\theta}^e$ and $J_{s,\theta}^o$ are the even- and odd-symmetric Log-Gabor quadrature pairs.

Given the complex phase $\phi_{s,\theta}(\underline{x})$, the complex phase order $R(\underline{x})$ can now be computed at each pixel to quantify the degree of complex phase alignment across all scales. In the original formulation by Morrone and Owens [1], the complex phase order $R(\underline{x})$ was quantified based on the normalized weighted summation of cosine-weighted complex phase deviations from the mean complex phase $\bar{\phi}_\theta(\underline{x})$ across all scales,

$$R(\underline{x}) = \frac{\sum\limits_{\theta=1}^{\beta}\sum\limits_{s=1}^{\alpha} A_{s,\theta}(\underline{x})\Lambda(\underline{x})}{\sum\limits_{\theta=1}^{\beta}\sum\limits_{s=1}^{\alpha} A_{s,\theta}(\underline{x})}, \quad (4)$$

where,

$$\Lambda(\underline{x}) = \cos\left(\phi_{s,\theta}(\underline{x}) - \bar{\phi}_\theta(\underline{x})\right). \quad (5)$$

This approach to computing complex phase order has been further extended by Kovesi [4] to improve response sensitivity as well as robustness to noise using a hard thresholding approach, and subsequently improved using a bilateral soft-thresholding approach by Wong et al. [12] to maintain a continuous measure for complex phase order. Given that it improves upon previous measures, we will employ the complex phase order measure proposed by Wong et al. [12] as defined by

$$R(\underline{x}) = \frac{\sum\limits_{\theta=1}^{\beta}\sum\limits_{s=1}^{\alpha} W_\theta(\underline{x})A_{s,\theta}(\underline{x})\Lambda(\underline{x})}{\sum\limits_{\theta=1}^{\beta}\sum\limits_{s=1}^{\alpha} A_{s,\theta}(\underline{x})}, \quad (6)$$

where $W_\theta(\underline{x})$ is the bilateral weighting function for orientation θ. The bilateral weighting function can be expressed as a product of a weighting function $W_\nu(\underline{x})$ related to non-zero summations in uniform regions and a weighting function $W_\tau(\underline{x})$ related to the distribution of amplitude across scales,

$$W_\theta(\underline{x}) = W_\nu(\underline{x})W_\tau(\underline{x}), \quad (7)$$

where $W_\nu(\underline{x})$ controls noise penalization in uniform regions based on the median of the summations of phase deviations over the visual data $\bar{\varpi}$,

$$W_\nu(\underline{x}) = \frac{1}{1 + \exp\left[\zeta(\bar{\varpi} - \varpi(\underline{x}))\right]}, \quad (8)$$

where ζ is the W_ν gain factor, $\varpi(\underline{x}) = \sum\limits_{\theta=1}^{\beta}\sum\limits_{s=1}^{\alpha} W_\theta(\underline{x})A_{s,\theta}(\underline{x})\Lambda(\underline{x})$, $\bar{\varpi} = median\left(\varpi(\underline{x})|\forall\underline{x} \in f\right)$, and $W_\tau(\underline{x})$ controls penalization based on an estimate of how evenly distributed complex amplitude is across scales [4],

$$W_\tau(\underline{x}) = \frac{1}{1 + \exp\left[\epsilon\left(c - 1 + A_{max,\theta}(\underline{x})/\sum\limits_{s=1}^{\alpha} A_{s,\theta}(\underline{x})\right)\right]}. \quad (9)$$

where c is the frequency where $W_\tau = 0.5$, ϵ is the W_τ gain factor, and A_{max} is the maximum amplitude across the scales. The parameters $c = 0.4$ and $\epsilon = \zeta = 10$ are used as described in [12], as they were found empirically to provide strong results across a variety of image types. A MR volume and its corresponding complex phase order representation is shown in Fig. 1. The structural characteristics of the MR volume are well captured in the complex phase order representation, making it useful as the underlying representation or energy functional for computer vision tasks such as segmentation and registration.

Unfortunately, current formulations of complex phase order representation suffer from two major limitations, as shown in Fig. 2. First, noticeable structural degradation is exhibited in the complex phase order representations at high levels of noise, with representations constructed above $\sigma = 16\%$ largely unusable for many computer vision tasks due to significant structural degradation. This is due to the fact that under high levels of noise it is difficult to distinguish noise from visual detail using the thresholding scheme, hence resulting in important structural characteristics being removed as well. Second, the large-scale and fine-scale structural characteristics are integrated as a single entity, making it difficult to separate and analyze differently-scaled structural characteristics in the visual data. These two limitations motivate us to explore multi-scale approaches to producing complex phase order representations for robust computer vision applications.
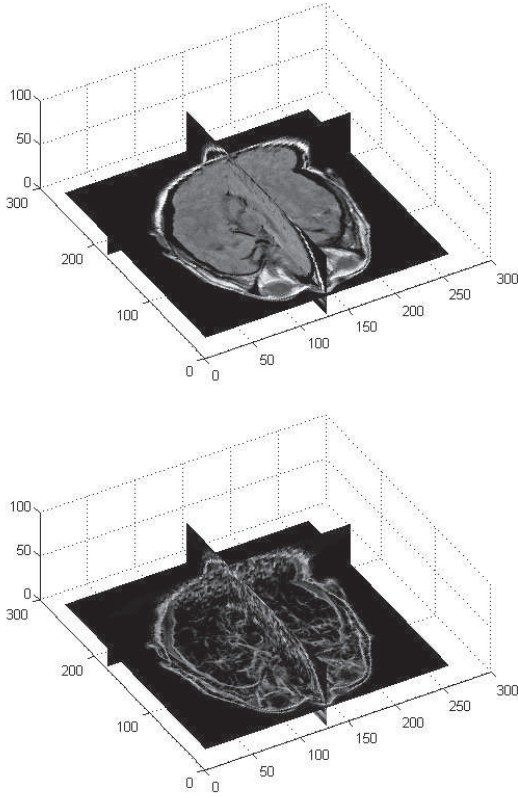
Fig. 1. A MR volume and its complex phase order representation. It can be observed that the structural characteristics of the MR volume are well captured.
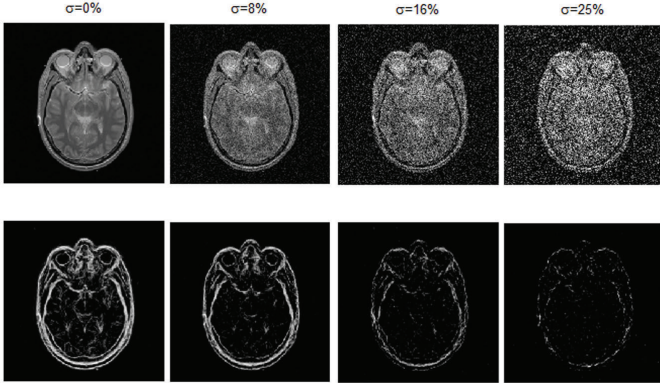

Fig. 2. The complex phase order representations of an axial slice from a MR volume under different noise scenarios (σ shown in terms of percentage of the dynamic range). The complex phase order representations suffer significant structural degradation under high noise scenarios.

III. MULTI-SCALE COMPLEX PHASE ORDER REPRESENTATIONS

One approach to addressing the two main limitations associated with the complex phase order representation described in Section II is to extend it into a multi-scale representation through the use of scale space theory. Scale space theory is a widely-used, powerful framework for handling the inherent multi-scale nature of visual data by representing visual data across multiple scales, with an increasing amount of fine-scale structures removed at each successive scale. One of the motivations for scale-space theory stems from the idea that, given no prior information about the scale of structures in the visual data, the only reasonable course of action is to represent the visual data at multiple pre-determined scales [19]. In scale space theory as first formalized by Witkin [20] and Koenderink and Van Doorn [21], visual data $f(\underline{x})$ is represented as a single-parameter family of derived visual data $L_t(\underline{x})$, where t is a scaling parameter that defines the scale of details being represented. At each scale t, all structures in the visual data smaller than a particular spatial size as governed by t are suppressed at the corresponding scale-space level. As such, scale space theory allows for the separation of structural characteristics at different scales, including noise, thus addressing the limitations.

Inspired by this, one can define a multi-scale complex phase order representation, denoted as $R_t(\underline{x})$, as

$$R_t(\underline{x}) = \frac{\sum\limits_{\theta=1}^{\beta} \sum\limits_{s=1}^{\alpha} W_{\theta,t}(\underline{x}) A_{s,\theta,t}(\underline{x}) \Lambda_t(\underline{x})}{\sum\limits_{\theta=1}^{\beta} \sum\limits_{s=1}^{\alpha} A_{s,\theta,t}(\underline{x})}, \tag{10}$$

where,

$$A_{s,\theta,t}(\underline{x}) = \sqrt{\left(L_t(\underline{x}) * J_{s,\theta}^e(\underline{x})\right)^2 + \left(L_t(\underline{x}) * J_{s,\theta}^o(\underline{x})\right)^2}, \tag{11}$$

and,

$$\phi_{s,\theta,t}(\underline{x}) = \tan^{-1}\left(\frac{L_t(\underline{x}) * J_{s,\theta}^e(\underline{x})}{L_t(\underline{x}) * J_{s,\theta}^o(\underline{x})}\right). \tag{12}$$

IV. DETERMINISTIC APPROACHES

Given the formulation of the multi-scale complex phase order representation in Section III, we will now explore the representation construction problem from a deterministic perspective. Deterministic multi-scale strategies for constructing multi-scale representations based on scale space theory generally fall into one of two categories: i) linear approach, and ii) nonlinear approach.

A. Linear approach

In the linear approach to multi-scale representations based on scale space theory, visual data is decomposed into a family of derived visual data based on a linear scale space operator. The most common linear approach is the Gaussian scale space approach first formalized by Witkin [20] and Koenderink and Van Doorn [21]. Given visual data $f(\underline{x})$, the linear scale space representation $L_t(\underline{x})$ is defined as the convolution of $L_0(\underline{x}) = f(\underline{x})$ and an isotropic Gaussian weighting function H_t,

$$L_t(\underline{x}) = \int\limits_{\underline{a}} H_t(\underline{a}) f(\underline{x} - \underline{a}) d\underline{a}, \tag{13}$$

$$H_t(\underline{a}) = \prod_{i=1}^{n} \frac{1}{\sqrt{2\pi t}} \exp\left[-\frac{a_i^2}{2t}\right]. \tag{14}$$

4

The main advantage of the linear approach is its computational and theoretical simplicity. Furthermore, the properties and characteristics of linear scale space theory has been well-studied [22], [23], [24].

The multi-scale complex phase order representation using the linear approach (Eq. (13)) of a slice from a MR volume are shown in Fig. 3. There are two observations that can be made that illustrate the fundamental limitation of multi-scale complex phase order representations constructed using the linear approach. First, the large-scale structures at coarse scales are poorly localized when compared to their true locations in the original visual data. Second, much of the corner information exhibited in the original visual data is lost at coarse scales. This makes extracting meaningful structural information at coarse scales for computer vision tasks very challenging. The significant structural degradation exhibited in the representation constructed using a linear approach is largely due to the fact that the linear scale space operator diffuses information in an isotropic fashion, regardless of the underlying characteristics of the visual data. As such, information from different structures are combined together, thus resulting in the poor structure localization and corner destruction.
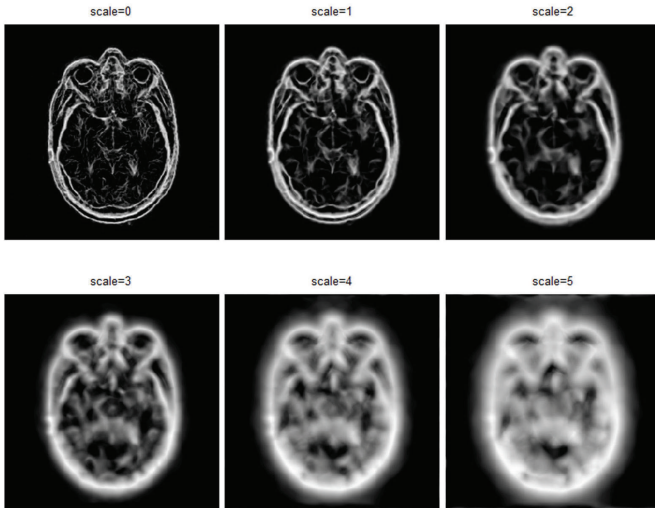

Fig. 3. Multi-scale complex phase order representation using a linear approach (Eq. (13)) of a slice from a MR volume at different scales. The large-scale structures at coarse scales are poorly localized when compared to their true locations in the original visual data.

B. Nonlinear approach

To address the limitations of the linear approach in Section IV-A, a new class of nonlinear approaches was introduced [25], [26], [27], [28], [29]. In the nonlinear approach to computing multi-scale representations using scale space theory, visual data is decomposed into a family of derived visual data based on a nonlinear scale space operator. Given that the limitations of the linear approach stem largely from the structure delocalizing and distorting nature of isotropic diffusion, a majority of existing nonlinear approaches extend

from the isotropic diffusion in a non-linear fashion to better localize meaningful structural information at coarse scales. Given a non-linear diffusion coefficient $c_t(\underline{x})$, the generalized diffusion equation can be expressed as,

$$\frac{\partial L}{\partial t} = c_t(\underline{x})\nabla^2 L + \nabla c_t(\underline{x}) \cdot \nabla L, \tag{15}$$

where ∇ is the gradient.

One of the most popular nonlinear approaches is that proposed by Perona and Malik [25], which proposed the use of a non-negative conduction coefficient in Eq. (15) that is a function of the gradient,

$$c_t(\underline{x}) = \exp\left[-\left(\frac{\nabla L_t(\underline{x})}{\kappa}\right)^2\right]. \tag{16}$$

where κ is the diffusion constant. This conduction coefficient possesses two important behavioral characteristics. First, the conduction coefficient preserves structures by limiting diffusion when the gradient is large, thus improving structural localization. Second, the conduction coefficient promotes intraregion smoothing by allowing for greater diffusion along the direction(s) perpendicular to image gradient, thus promotes structural separation between adjacent scales.

The multi-scale complex phase order representations based on the nonlinear approach for a slice from a MR volume are shown in Fig. 4. The structures are noticeably better localized when compared to the linear approach at coarse scales. Unfortunately, the structures at the coarser scales starts to become delocalized and the corner information becomes lost as with the case of the linear approach. This structural degradation at coarser scales is largely due to the fact that the nonlinear approach relies entirely on information within a local neighborhood, which is insufficient for maintaining structural detail at the coarser scales.

Given that the major limitations of the deterministic approaches are associated with the limitations of using just information within a local neighborhood, one is motivated to explore alternative multi-scale approaches that is able to utilize information throughout the entire visual data to provide better structural localization at coarse scales and greater resilience to noise.

V. BAYESIAN THEORETIC APPROACH

To explore alternative approaches for constructing multi-scale complex phase order representations, let us study the construction of multi-scale representations within a Bayesian theoretic framework. One can view the relationship between a scale representation $L_t(\underline{x})$ and the visual data $f(\underline{x})$ as an additive relationship, which can be expressed by

$$f(\underline{x}) = L_t(\underline{x}) + N_t(\underline{x}), \tag{17}$$

where $N_t(\underline{x})$ is the scale residual, and $L_0(\underline{x}) = f(\underline{x})$. As the scaling parameter t increases, the energy associated with the scale residual N_t increases while the energy associated with the scale representation L_t decreases. Based on Eq. (17), the problem of constructing multi-scale representations can
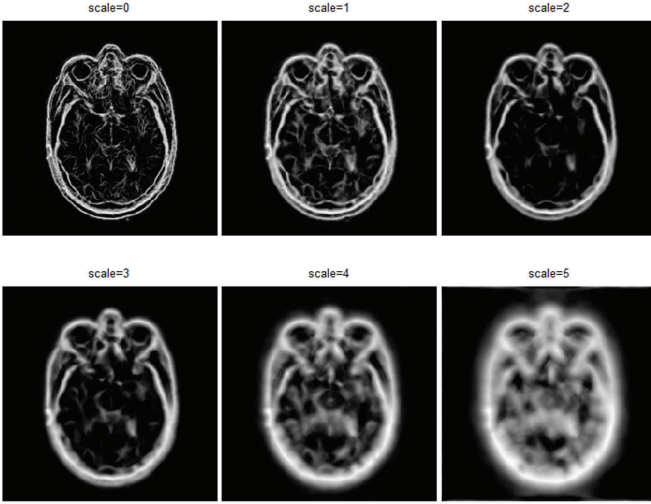
Fig. 4. Multi-scale complex phase order representation using a nonlinear deterministic approach (Eq. (15)) of a slice from a MR volume at different scales. The structures are noticeably better localized at coarse scales when compared to the linear approach. Unfortunately, the structures at the coarser scales starts to become delocalized and the corner information becomes lost as with the case of linear approach.

be viewed as a series of inverse source separation problems, where each problem involves separating a scale representation $L_t(\underline{x})$ from the scale residual $N_t(\underline{x})$ given the visual data $f(\underline{x})$. One possible strategy of solving this series of inverse source separation problems is to estimate $L_t(\underline{x})$ at each scale using a Bayesian theoretic framework.

Let $\underline{X}$ be a set of sites into a discrete lattice $\mathcal{L}$ and $\underline{x} \in \underline{X}$ be a site in $\mathcal{L}$. Let $L_t = \{L_t(\underline{x})|\underline{x} \in \underline{X}\}$, $f = \{f(\underline{x})|\underline{x} \in \underline{X}\}$, and $N_t = \{N_t(\underline{x})|\underline{x} \in \underline{X}\}$ be random fields on $\underline{X}$, with $L_t(\underline{x})$, $f(\underline{x})$, and $N_t(\underline{x})$ taking on values representing the state at site $\underline{x}$ and scale t, observation at site $\underline{x}$, and residual at site $\underline{x}$ and scale t, respectively. Based on the relationship expressed in Eq. (17), we model the source separation problem at scale t as a Bayesian least squares problem [30],

$$\hat{L}_t(\underline{x}) = \underset{L_t(\underline{x})}{\arg\min} \left\{ E\left[\left(L_t(\underline{x}) - \hat{L}_t(\underline{x})\right)^2 | f(\underline{x}) \right] \right\}. \quad (18)$$

Within this Bayesian least squares problem formulation, the optimal estimate of the representation $L_t(\underline{x})$ can be computed as the conditional expected value of $L_t(\underline{x})$ given $f(\underline{x})$, denoted as $\mathrm{E}(L_t(\underline{x})|f(\underline{x}))$ [30],

$$\hat{L}_t(\underline{x}) = \mathrm{E}(L_t(\underline{x})|f(\underline{x})) = \int L_t(\underline{x}) p(L_t(\underline{x})|f(\underline{x})) \, \mathrm{d}L_t(\underline{x}), \quad (19)$$

where $L_0(\underline{x}) = f(\underline{x})$, and can be solved in practice via numerical integration [31]. The main challenge to computing the conditional expected value $\mathrm{E}(L_t(\underline{x})|f(\underline{x}))$ as formulated in Eq. (19) is the computation of the posterior distribution $p(L_t(\underline{x})|f(\underline{x}))$. In practice, one approach to computing an empirical approximation of the posterior distribution is to utilize all samples from f within a small local neighborhood around site $\underline{x}$. However, this can lead to a poor approximation of $p(L_t(\underline{x})|f(\underline{x}))$ due to two main limitations:

1) High sample proximity bias: Given that the samples used are obtained from a small local neighborhood around $\underline{x}$, the approximation of $p(L_t(\underline{x})|f(\underline{x}))$ becomes overly biased towards samples within very close proximity to $\underline{x}$. This can lead to poor structural localization in the constructed multi-scale complex phase order representations as the information within a local neighborhood is insufficient for maintaining structural detail at the coarser scales.

2) High noise sensitivity: Given that the number of samples used to approximate $p(L_t(\underline{x})|f(\underline{x}))$ is very small given that only information within a local neighborhood is used, the approximation of $p(L_t(\underline{x})|f(\underline{x}))$ is highly sensitive to the presence of noise, which can result in poor noise resilience in the constructed multi-scale complex phase order representations.

Given that both issues associated with the existing deterministic approaches are due to the limitations of using only information within a local neighborhood, one is motivated to extend the approximation of $p(L_t(\underline{x})|f(\underline{x}))$ to utilize information from the entire f. However, using the entire f can be very computationally demanding. Here, we instead compute a Bayesian approximation of $p(L_t(\underline{x})|f(\underline{x}))$ using a rejection sampling approach, where random samples are drawn from f and used to compute the approximation. The main advantage of such an approach is that it allows for computationally efficient approximation of $p(L_t(\underline{x})|f(\underline{x}))$ while still attaining similar benefits of using information from throughout the entire visual data.

A. Rejection Sampling

The proposed rejection sampling strategy for approximating $p(L_t(\underline{x})|f(\underline{x}))$ can be described as follows. First, we draw a random pixel position $\underline{\xi}$ from an instrumental distribution, $q(\underline{\xi}|\underline{x})$, given as

$$q(\underline{\xi}|\underline{x}) = \frac{exp\left[-\left|\underline{x} - \underline{\xi}\right|^2 \left(\sigma^2(\underline{\xi}) - \sigma^2(\underline{x})\right)^2\right]}{\sum_{\underline{\xi}} exp\left[-\left|\underline{x} - \underline{\xi}\right|^2 \left(\sigma^2(\underline{\xi}) - \sigma^2(\underline{x})\right)^2\right]}, \quad (20)$$

where $\sigma^2(\cdot)$ is the variance of the local neighborhood around $\underline{x}$ and $|\cdot|$ is the Euclidean distance. The distribution $q(\underline{\xi}|\underline{x})$ takes care of the proximity to position $\underline{x}$ and the statistical similarity between the two positions measured by the difference of corresponding $\sigma^2(\cdot)$. The instrumental distribution $q(\underline{\xi}|\underline{x})$ promotes the drawing of samples that are within closer spatial proximity and have higher statistical similarity, which are more likely to share useful information related to $\underline{x}$.

While the instrumental distribution q promotes samples with higher statistical similarity and closer spatial proximity to $\underline{x}$, there is no guarantee that the samples have high data similarity. To further improve the likelihood of high data similarity, the data similarity between the sample $\underline{\xi}$ drawn from the instrumental distribution q and $\underline{x}$ is then evaluated based on the cumulative Gaussian-weighted squared gradient between the local neighborhoods $\mathcal{N}_{\underline{x}}$ and $\mathcal{N}_{\underline{\xi}}$,

6

$$\nabla_{\mathcal{N}}(\underline{\xi}, \underline{x}) = \sum_{\mathcal{N}} H(\mathcal{N}) \cdot \left(f(\mathcal{N}_{\underline{\xi}}) - f(\mathcal{N}_{\underline{x}}) \right)^2, \qquad (21)$$

where H is the Gaussian kernel, and high values of $\nabla_{\mathcal{N}}$ indicate low data similarity. Based on Eq. (21), the sample $\underline{\xi}$ is employed for the approximation of $p(L_t(\underline{x})|f(\underline{x}))$ if

$$\nabla_{\mathcal{N}}(\underline{\xi}, \underline{x}) < \tau, \qquad (22)$$

where τ is the rejection constant. The rejection sampling process is repeated until an upper bound for sampling q has been reached, resulting in the final set of m samples $\underline{\xi}_1, \ldots, \underline{\xi}_m$ for approximating $p(L_t(\underline{x})|f(\underline{x}))$.

B. Importance weighted posterior approximation

After the m samples $\underline{\xi}_1, \ldots, \underline{\xi}_m$ are drawn during the rejection sampling process, $p(L_t(\underline{x})|f(\underline{x}))$ can be approximated based on an importance weighted approximation approach, where the approximation of $p(L_t(\underline{x})|f(\underline{x}))$ can be formulated as the following weighted histogram,

$$p(L_t(\underline{x})|f(\underline{x})) = \frac{\sum_{i=1}^m w_t(\underline{\xi}_i|\underline{x})\delta(f(\underline{x}) - f(\underline{\xi}_i))}{\sum_{i=1}^m w_t(\underline{\xi}_i|\underline{x})}, \qquad (23)$$

where δ is the Dirac delta and $w_t(\underline{\xi}|\underline{x})$ is a importance weighting function indicating the contribution of $\underline{\xi}$ on the approximation process. The importance weighting function $w_t(\underline{\xi}|\underline{x})$ should achieve three important goals. First, the weighting function should maintain structural localization and avoid structural degradation at coarse scales. Second, the weighting function should provide good effective noise resilience such that the resulting multi-scale complex phase order representation is minimally influenced by the presence of noise at all scales. Third, the weighting function should remove structural information from the image in a monotonic fashion as the scale increases. As such, the importance weighting function used in approximating $p(L_t(\underline{x})|f(\underline{x}))$ for the construction of the multi-scale complex phase order representation needs to be designed to achieve all three goals.

Recall that to maintain structural localization and avoid structural degradation at coarse scales while suppressing noise at fine scales, a nonnegative exponential conduction coefficient (Eq. (16)) was introduced in the nonlinear approach proposed by Perona and Malik [25]. Interpreting the conduction coefficient as an importance weighting function, the contribution of a sample $\underline{\xi}$ to the approximation of $p(L_t(\underline{x})|f(\underline{x}))$ is proportional to the gradient. Inspired by this conduction coefficient while motivated to further improve structural localization and noise resilience, an importance weighting function $w_t(\underline{\xi}|\underline{x})$ is employed based on the concept of squared neighborhood gradient $\nabla_{\mathcal{N}}$,

$$w_t(\underline{\xi}|\underline{x}) = \exp\left[-\left(\frac{\nabla_{\mathcal{N}}(\underline{\xi}, \underline{x})}{\varphi t} \right) \right], \qquad (24)$$

where the neighborhood squared gradient $\nabla_{\mathcal{N}}$ is defined as the cumulative Gaussian-weighted squared gradient between

the local neighborhoods $\mathcal{N}_{\underline{x}}$ and $\mathcal{N}_{\underline{\chi}}$ as defined in Eq. (21), and φ is the diffusion multiplier constant.

Based on the m samples $\underline{\xi}_1, \ldots, \underline{\xi}_m$ drawn and the importance weighting function $w_t(\underline{\xi}_i|\underline{x})$ from Eq. (24), an approximation of $p(L_t(\underline{x})|f(\underline{x}))$ is computed according to Eq. (23), which is then used to compute $L_t(\underline{x})$ according to Eq. (19). Finally, $R_t(\underline{x})$ is computed according to Eq. (10). The pseudo-code for the proposed Bayesian theoretic approach to constructing multi-scale complex phase representations is presented in Algorithm 1.

Algorithm 1 Proposed approach

Require: Given $f(\underline{x})$, $t = 0$
1:   $L_0(\underline{x}) = f(\underline{x})$.
2:   Compute $R_0(\underline{x})$ according to (10).
3:   **repeat**
4:      $t = t + 1$.
5:      $k = 0$.
6:      **repeat**
7:         $k = k + 1$.
8:         Draw a random sample $\underline{\xi}$ based on $q(\underline{\xi}|\underline{x})$ (20).
9:         Reject sample if (22) is not met. Otherwise accept into set of samples.
10:     **until** $k = k_{\max}$
11:     Based on the accepted samples, estimate $p(L_t(\underline{x})|f(\underline{x}))$ according to (23).
12:     Compute $L_t(\underline{x})$ according to (19).
13:     Compute $R_t(\underline{x})$ according to (10).
14:   **until** $t = t_{\max}$
15:   **return** $R(\underline{x})$.

The multi-scale complex phase order representations based on the Bayesian theoretic approach for a slice from a MR volume are shown in Fig. 5, with the upper bound for sampling $k_{\max}$ set to a maximum of 100 iterations. The structures are significantly better localized using the Bayesian theoretic approach when compared to the linear and nonlinear deterministic approaches at coarse scales. This improved structural localization at coarser scales is largely due to the fact that the Bayesian theoretic approach takes advantage of the global information within the visual data to better maintain structural detail at the coarser scales.

VI. EXPERIMENTAL RESULTS

The goal of this section is to investigate the effectiveness of the proposed Bayesian theoretic approach to constructing multi-scale complex phase order representations with strong structural localization and noise resilience. To achieve this goal, a number of experiments using visual data volumes acquired from the NLM Visible Human Project, with example slices from each test volume shown in Fig. 6. For comparison purposes, multi-scale complex phase order representations were also constructed using the linear deterministic approach described in Section IV-A and the nonlinear deterministic approach described in Section IV-B, with all parameters set based on their respective literatures. Furthermore, for the Bayesian theoretic approach, the upper bound for sampling $k_{\max}$ was set to a maximum of 100 iterations, $\varphi = 0.02$, and τ was set based on the median local variance ($\tau = \frac{1}{2}\sigma_{\mathrm{med}}^2$) as it was shown to produce strong multi-scale representations during testing. Finally, the local neighborhoods used are 9×9 rectangular neighborhoods.

This article has been accepted for publication in a future issue of this journal, but has not been fully edited. Content may change prior to final publication.

WONG   7
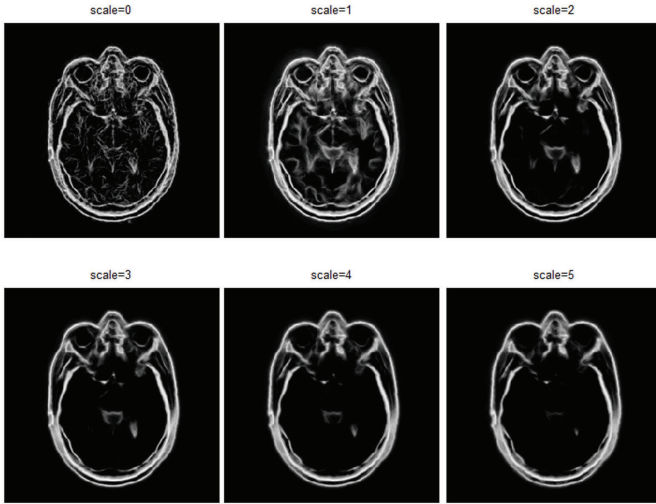
Fig. 5. Representation constructed using Bayesian theoretic approach (Eq. (19)) of a slice from a MR volume at different scales. The structures in the representations constructed using the Bayesian theoretic approach are significantly better localized at coarse scales when compared to that constructed using the linear and nonlinear deterministic approaches.
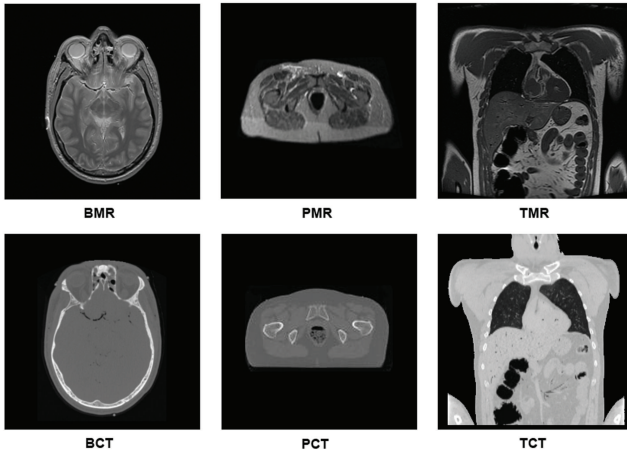
Fig. 6. Sample slices from the test volumes.

A. Structural Localization

Since one of the main goals for the design of the multi-scale complex phase order representation is to maintain strong structural localization, it is important to study the localization of structures at different scales. Given the multi-scale complex phase order representations constructed using the three tested methods, it is necessary to design a measure of structural localization in order to perform a quantitative analysis between the different methods. To achieve strong structural localization, the locations of structures at any given scale should also coincide with their locations in the lowest scale. Therefore, intuitively, all structural information at a particular scale that does not exist at the lowest scale is considered a result of structural delocalization. Motivated by this, an effective measure of structural delocalization, ϵ, for a multi-scale complex phase order representation at a particular scale t can be defined

as the cumulative structural significance of structures that do not coincide with existing structures at the lowest scale, normalized by the quantity of total structures at the lowest scale,

$$\epsilon\left(t\right) = \frac{\sum\limits_{\underline{x}, R_0(\underline{x})=0} R_t(\underline{x})}{\sum\limits_{x}\{R_0(\underline{x}) > 0\}}. \tag{25}$$

This can be interpreted as the proportion of structural information in scale space that do not have a correspondence in the original image. The structural delocalization ϵ of the multi-scale complex phase order representations for the test sets at different scales t are shown in Fig. 7. The structural delocalization of the multi-scale complex phase order representations constructed using the linear and nonlinear deterministic approaches increases significantly as scale increases. On the other hand, the structural delocalization of the representations constructed using the Bayesian theoretic approach remains relatively low and constant at all scales for all test sets. What this means is that the Bayesian theoretic approach provides multi-scale complex phase order representations with improved structural localization at all scales when compared to the other two approaches.

The multi-scale complex phase order representations of the PMR test set at different scales are shown in Fig. 8 respectively. The structural characteristics are significantly better localized in the multi-scale complex phase order representations produced using the Bayesian theoretic approach at coarse scales when compared to that produced using the linear and nonlinear deterministic approaches. This improved structural localization at coarser scales is largely due to the fact that the Bayesian theoretic approach takes advantage of the global information within the visual data to better preserve the true location of structures at the coarser scales.

B. Noise Sensitivity

To study the effects of noise on the multi-scale complex phase order representations, additive Gaussian noise was applied with standard deviations of $\sigma = \{8\%, 16\%, 22\%, 25\%\}$ to the test sets. To provide a quantitative assessment of the noise sensitivity of the multi-scale complex phase order representations at fine scales, the peak signal-to-noise ratio (PSNR) and the mean Structural Similarity (MSSIM) [32] were measured between the complex phase order representations at scale $t = 1$ with and without noise. The noise sensitivity analysis was performed at scale $t = 1$ for two main reasons. First, the influence of noise on representations are most prominent at fine scales, thus making it representative of the noise resilience of a multi-scale complex phase order representation. Second, the structural localization at that scale remains similar across all approaches, thus allowing for a fair comparison of noise sensitivity between the different multi-scale complex phase order representations. The PSNR and MSSIM results for the complex phase order representation described in Section III is shown as a baseline reference.

The PSNR and MSSIM results for the test sets are shown in Fig. 9. The PSNR and MSSIM is noticeably higher for
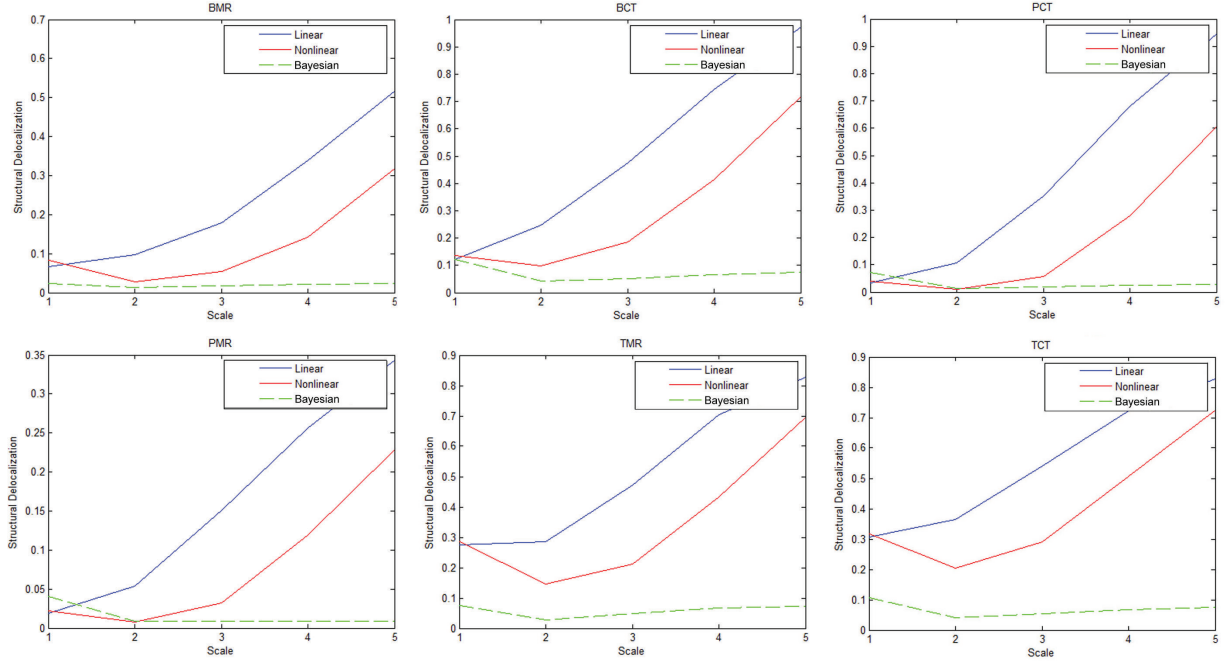
8

Fig. 7. Plots of the structural delocalization ϵ of the multi-scale complex phase order representations for the test sets (Fig. 6) at different scales.

the multi-scale representations for all noise scenarios than the baseline reference complex phase order representation, thus illustrating the gain in noise resilience when multi-scale representations are used. Furthermore, the PSNR and MSSIM of the Bayesian theoretic approach is noticeably higher than the linear and nonlinear deterministic approaches, hence demonstrating improved noise resilience over the other approaches. The multi-scale complex phase order representations of the BMR image under the tested noise scenarios using linear and nonlinear deterministic approaches, and the Bayesian theoretic approach are shown in Fig. 10. While increasing structural degradation is exhibited in all of the tested multi-scale complex phase order representations as the level of noise increases, the Bayesian theoretic approach is able to better preserve structural detail at high noise levels when compared to the other tested approaches.

VII. ILLUSTRATIVE APPLICATION: MULTIMODAL REGISTRATION

Given that the proposed Bayesian theoretic approach to constructing multi-scale complex phase order representation allows for the capturing of structural characteristics of visual data largely independent of intensity, a computer vision application that it is very well suited for is multimodal image registration, where the goal is to align images acquired under different conditions (e.g., different perspectives, lighting conditions, imaging technologies, etc.) The multimodal registration problem can be formulated as a maximization problem,

$$T_{\text{opt}} = \text{argmax}_T \left[\Psi \left(g(\underline{x}), f(T(\underline{x})) \right) \right], \qquad (26)$$

where T_{opt} is the optimal transformation that aligns f and g, and $\Psi(.)$ is the objective function. To incorporate the

multi-scale complex phase order representation described in Section V into Eq. (26), we introduce the following multi-scale complex phase representation (MCPR) objective function based on the Geman-McClure statistics [33] between the multi-scale complex phase order representations between f and g,

$$\Psi \left(g(\underline{x}), f(T(\underline{x})) \right) = \exp \left[- \left(\sum_{t=1}^{\gamma} \sum_{\underline{x}} \frac{(R_{g,t}(\underline{x}) - R_{f,t}(T(\underline{x})))^2}{\chi^2 + (R_{g,t}(\underline{x}) - R_{f,t}(T(\underline{x})))^2} \right) \right]. \tag{27}$$

To study the performance of the proposed MCPR objective function under more complex scenarios, volumetric registration using 9 real patient MR-CT brain volume data sets from the Whole Brain Atlas [34] (WBA) was performed under different scenarios. The MR volumes are $256 \times 256 \times 23$ voxels, with a slice thickness of 5mm. The CT volumes are downsampled to the same voxel dimensions. A summary of each test data set is given below.

1) **Test 1**: MR/PD-CT, 63 year-old male.
2) **Test 2**: MR/T2-CT, 63 year-old female.
3) **Test 3**: MR/T2-CT, 45 year-old female.
4) **Test 4**: MR/T2-CT, 23 year-old female.
5) **Test 5**: MR/PD-CT, 42 year-old female.
6) **Test 6**: MR/PD-CT, 75 year-old male.
7) **Test 7**: MR/T2-CT, 22 year-old male.
8) **Test 8**: MR/T2-CT, 55 year-old male.
9) **Test 9**: MR/T2-CT, 71 year-old female.

For testing the objective functions, the following volumetric registration algorithm was used. Given the optimization problem for multimodal image registration described in Eq. (26), a sequential quadratic programming approach [35] is then
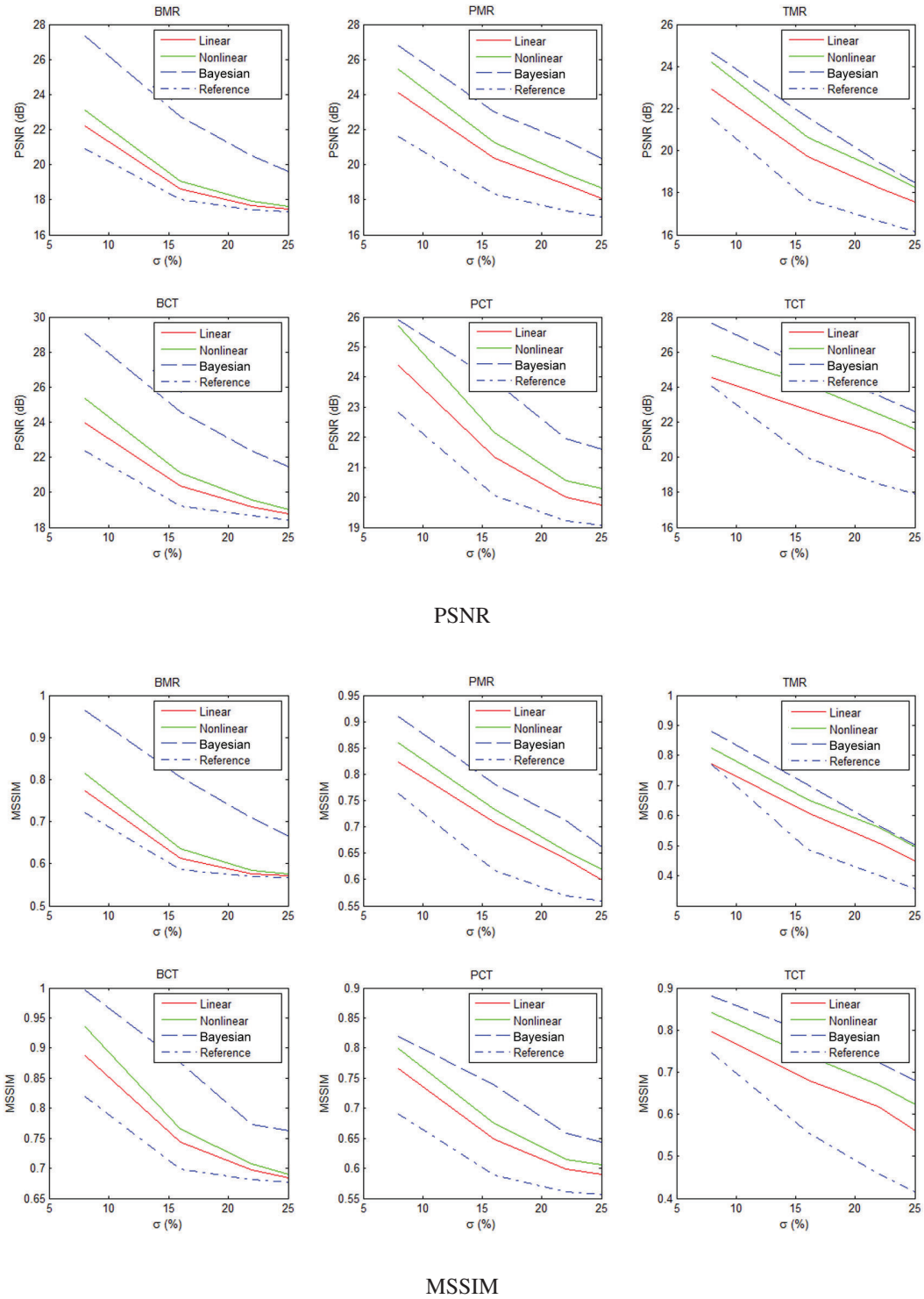
Fig. 9. Plots of the PSNR for the test sets under different noise scenarios. The PSNR and MSSIM are noticeably higher for the multi-scale representations for all noise scenarios than the baseline reference complex phase order representation, thus illustrating the gain in noise resilience. Furthermore, the PSNR and MSSIM of the Bayesian theoretic approach are noticeably higher than the linear and nonlinear deterministic approaches.

Linear

σ=8% σ=16% σ=22% σ=25%

Nonlinear

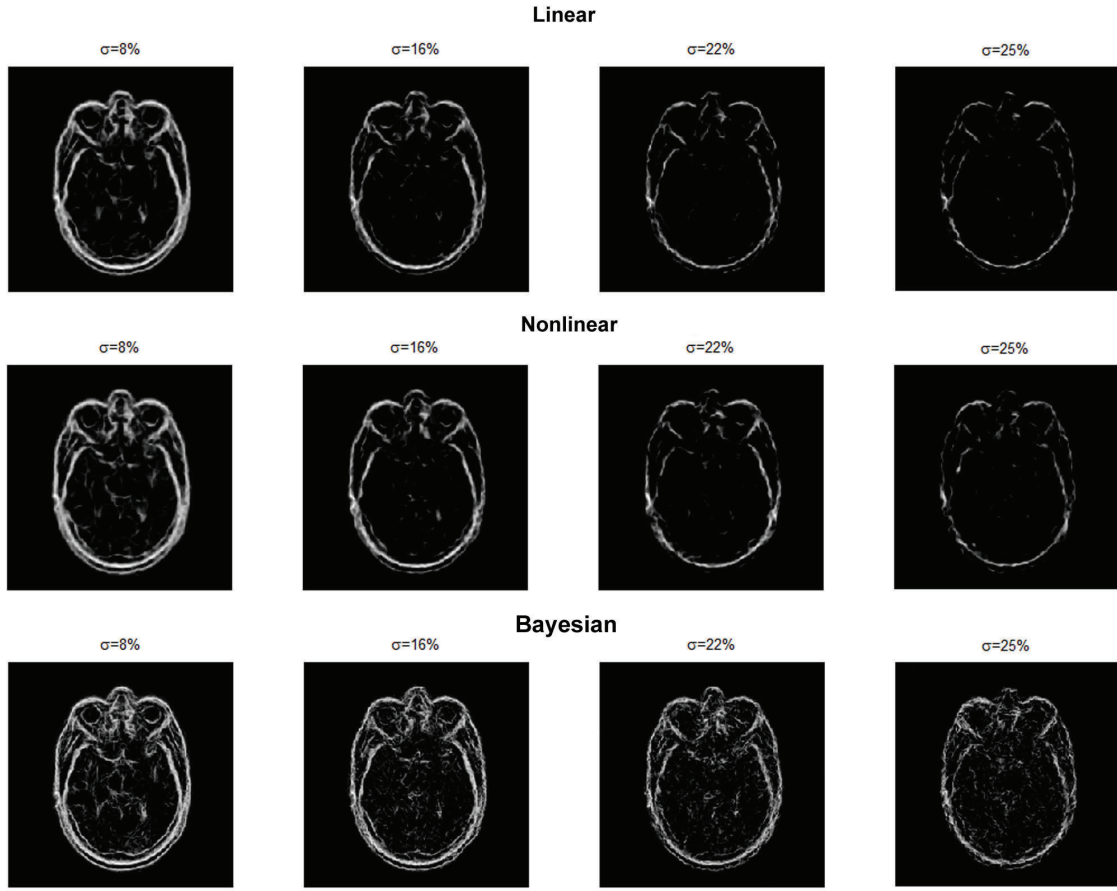σ=8% σ=16% σ=22% σ=25%

Bayesian

σ=8% σ=16% σ=22% σ=25%

Fig. 10. The multi-scale complex phase order representations of the BMR image under the tested noise scenarios. When compared to the complex phase order representations shown in Fig. 2, it can be observed that the Bayesian theoretic approach provides significantly better noise robustness at high noise levels while maintaining strong structural detail preservation.

employed to solve the problem, where the estimated transformation $\hat{T}$ at iteration k can be defined as

$$\hat{T}_k = \hat{T}_{k-1} + \gamma_{k-1} d_{k-1}, \qquad (28)$$

where γ is a non-negative step size and d is the step direction calculated by solving a quadratic subprogram involving Ψ [35]. The pseudo-code for registering two volumes f and g is presented in Algorithm 2.

Algorithm 2 Volumetric Registration

Require: Given $T_0 = I$, $k = 0$
1: **repeat**
2:     Compute $\Psi(g(\underline{x}), f(T_k(\underline{x})))$ (27).
3:     $k = k + 1$.
4:     Estimate $\hat{T}_k$ (28).
5: **until** $\triangle\Psi < \epsilon_{convergence}$
6: **return** $\hat{T}_k$.

For evaluation purposes, the normalized mutual information (NMI) [36], the complex phase order likelihood (CPOL) [12], and MCPR objective functions were tested. NMI was implemented using smoothed histograms computed with 100 intensity bins as specified by Mellor and Brady [37]. Trilinear interpolation was used in all experiments. All tests were performed on an Intel Core 2 Duo 1.67 GHz PC with 2 GB of RAM and implemented using MATLAB, with the registration time of MCPR was approximately 4 minutes.

A. Registration under Noise-free Conditions

The first set of tests studies the registration accuracy using NMI, CPOL, and MCPR under geometric distortion scenarios. Each test data set was distorted using 30 randomly generated affine transformations, based on the random perturbation of translation coefficients up to ± 30mm and all other coefficients up to ± 0.1, resulting in a total of 270 test cases. Since the test image sets used were previously aligned, the gold-standard transformations are known for all 270 test cases. Registration accuracy for all methods is evaluated quantitatively based on the fiducial registration error (FRE), which in our case can be defined by the root-mean-square error of 60 fiducial points within the region of interest. Furthermore, since the test image sets used were previously aligned and thus corresponding locations on the images are known, the fiducial points were
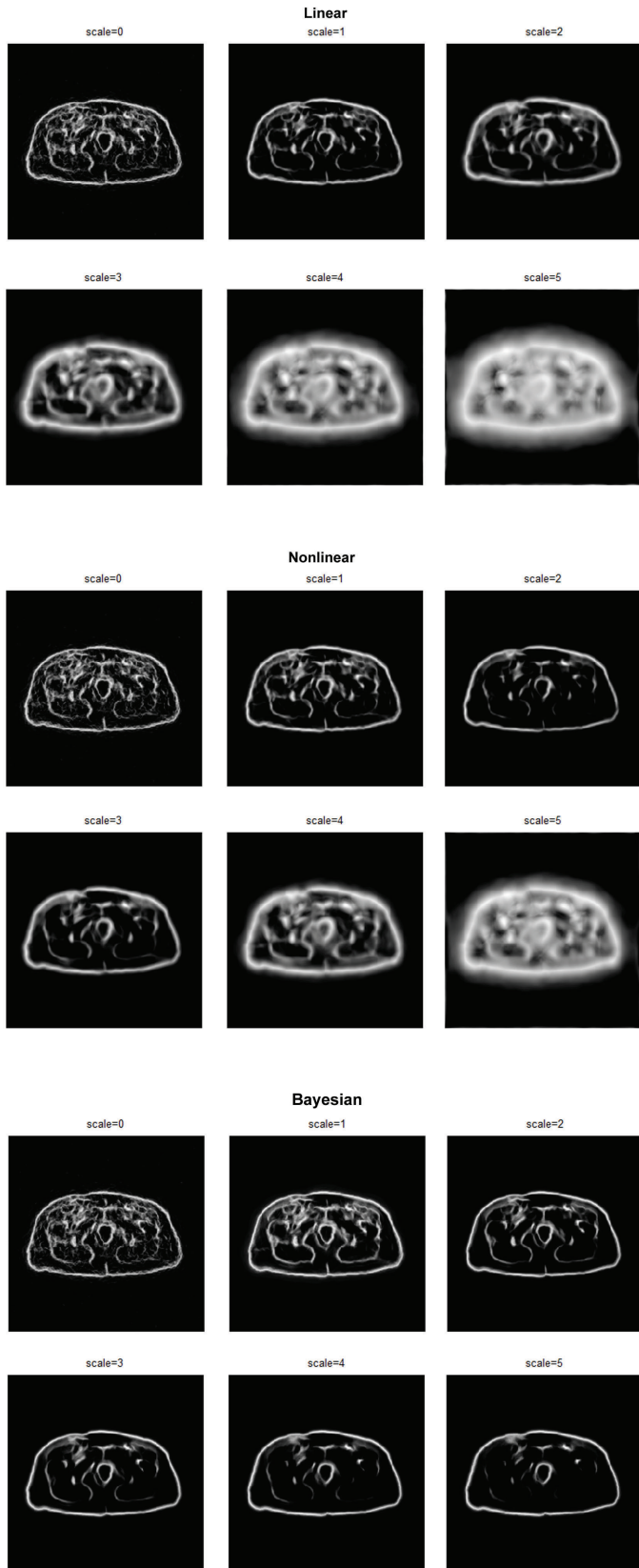
Fig. 8. The multi-scale complex phase order representations of the PMR test set at different scales. The structural characteristics are significantly better localized in the multi-scale complex phase order representations produced using the Bayesian theoretic approach at coarse scales when compared to that produced using the linear and nonlinear deterministic approaches.

chosen randomly using a computerized random point generation algorithm within the regions of interest in the test images as not to bias the tests towards any of the tested similarity measures.

The registration results for all nine test data sets, totalling 270 test cases, are summarized in Table I. Both CPOL and MCPR were capable of achieving noticeably lower FRE when compared to NMI for all test cases. One contributing factor to this difference in registration error when compared to NMI is that the intensity relationships between the tested MR and CT volume data sets are highly complex and nonlinear, making NMI highly non-convex and difficult to optimize. On the other hand, the structural relationships between the volume data sets is significantly more straightforward, making CPOL and MCPR more straightforward to optimize. Furthermore, MCPR produced lower FRE when compared to CPOL for all test cases. Sample registration results using MCPR for Test 1 shown in Fig. 11. Visually, MCPR was capable of providing accurate registration results. These experimental results demonstrate the effectiveness of the MCPR objective function for performing non-rigid multimodal image registration on CT and MR images.

TABLE I
FIDUCIAL REGISTRATION ERRORS (FRE) OF NMI, CPOL, AND MCPR FOR THE 9 DATA SETS. A TOTAL OF 30 RANDOM DISTORTIONS IS TESTED FOR EACH DATA SET, FOR A TOTAL OF 270 TEST CASES.

Test Set	FRE (mm)		
	NMI	CPOL	MCPR
Test 1	3.74±0.56	2.70±0.32	**2.21**±0.29
Test 2	3.91±0.50	2.24±0.37	**2.09**±0.34
Test 3	2.36±0.63	2.46±0.42	**2.31**±0.43
Test 4	3.64±0.49	2.19±0.35	**2.08**±0.27
Test 5	3.81±0.30	2.46±0.19	**2.31**±0.22
Test 6	3.71±0.47	2.59±0.27	**2.40**±0.28
Test 7	2.90±0.53	2.70±0.25	**2.57**±0.20
Test 8	3.35±0.55	2.48±0.29	**2.39**±0.23
Test 9	3.97±0.61	2.30±0.37	**2.12**±0.35

B. Registration under Noise

An important consideration in the design of an objective function for image registration is that the objective function should be robust to noise artifacts that can affect registration accuracy. To study the effect of noise on the similarity measures, the set of tests conducted in Section VII-A for Test 1 were performed with the MR volumes contaminated by 5%, 10%, 15%, and 20% simulated Rician noise, resulting in a total of 120 tests.

The registration results for the Test 1 under the various noise levels, totalling 120 test cases, are summarized in Table II. The FRE achieved using MCPR remained largely consistent at all noise levels. On the other hand, the FRE achieved using NMI rose significantly as noise levels increased, while the FRE achieved using CPOL were noticeably higher than that achieved using MCPR, particularly for high noise levels. This difference in FRE can be primarily contributed to the noise robust nature of the complex phase order representations used in MCPR when compared to that used in CPOL, which suffers

12

Before Registration　　　　**MCPR**
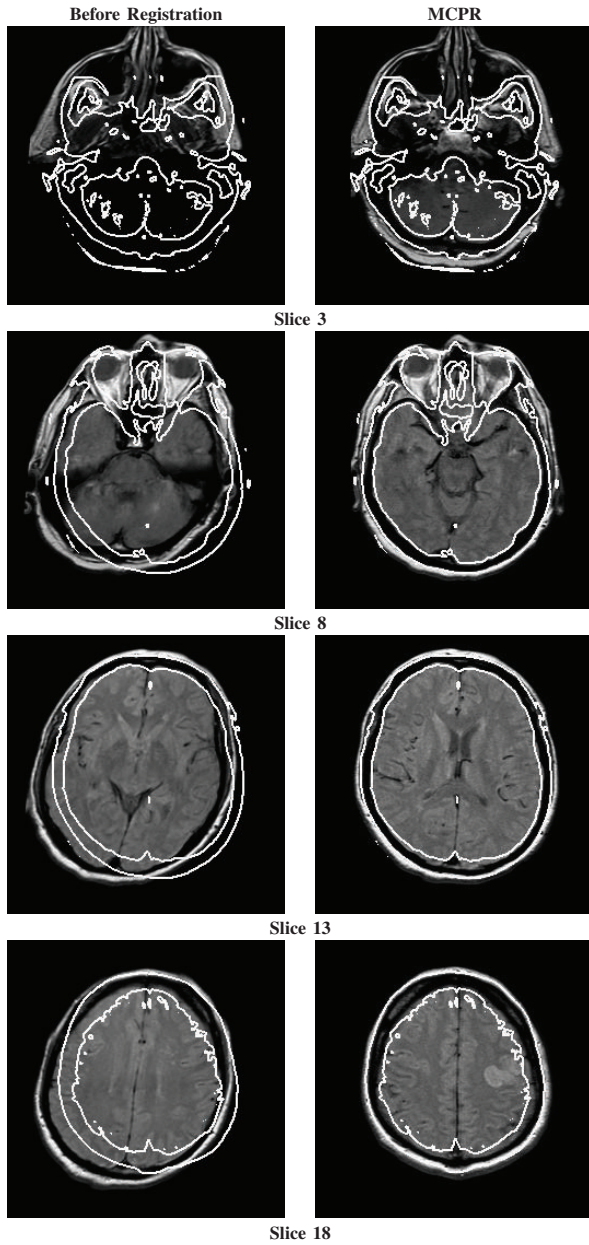
Slice 3

Slice 8

Slice 13

Slice 18

Fig. 11. Sample registration result from Test 1 using MCPR. For visualization, slices from the volumes are shown. Contours extracted from the CT volume are overlayed on the MR volume to visualize the quality of registration. Visually, the MR volumes warped based on MCPR appear well aligned with the CT volume.

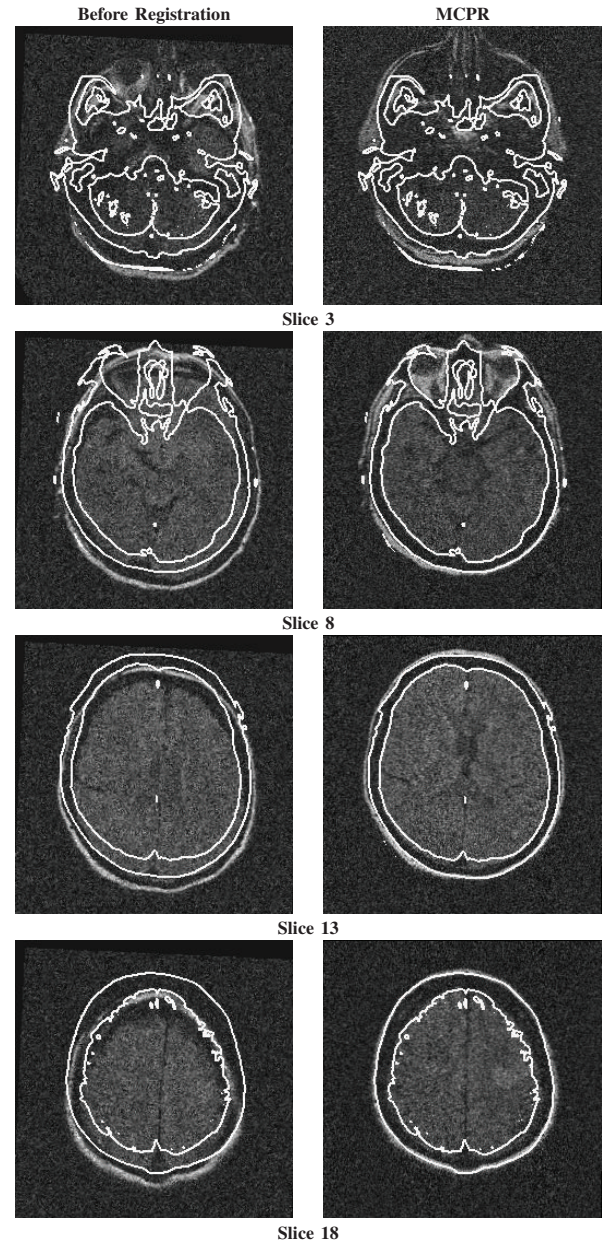**Before Registration**　　　　**MCPR**

Slice 3

Slice 8

Slice 13

Slice 18

Fig. 12. Sample registration result from Test 1 using MCPR under 20% Rician noise. For visualization, corresponding slices from the volumes are shown. Contours extracted from the CT volume are overlayed on the MR volume to visualize the quality of registration. Visually, the MR volume warped based on MCPR appears well aligned with the CT volume despite noise.

significant degradation under high noise scenarios. Sample registration results using NMI and MCPR for 20% simulated Rician noise are shown in Fig. 12. Visually, MCPR is capable of providing accurate registration results. These experimental results demonstrate the robustness of MCPR to the presence of noise artifacts.

VIII. ILLUSTRATIVE APPLICATION: ULTRASOUND FEATURE EXTRACTION

Given that the proposed Bayesian theoretic approach to constructing multi-scale complex phase order representation allows for the capturing of structural characteristics under high noise levels, another potential application is the extraction of features from ultrasound imagery [38], [11], which is highly contaminated by the presence of speckle noise. To illustrate the potential of the proposed Bayesian theoretic approach for extracting features from ultrasound imagery, Fig. 13 shows the average multi-scale complex phase order representation produced using the Bayesian theoretic approach across all scales for a real-world ultrasound image of the prostate, which exhibits heavy speckle noise contamination. It can be observed that the structural characteristics of the prostate gland are

TABLE II

FIDUCIAL REGISTRATION ERRORS (FRE) OF NMI AND MCPR FOR TEST 1 UNDER DIFFERENT RICIAN NOISE LEVELS FOR MR VOLUME. A TOTAL OF 30 RANDOM DISTORTIONS IS TESTED FOR EACH NOISE LEVEL, FOR A TOTAL OF 120 TEST CASES.

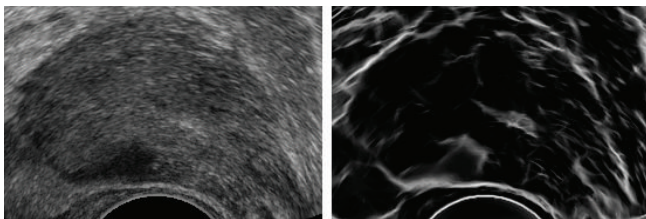| Rician noise	FRE (mm)			
	5%	10%	15%	20%
NMI	4.02±0.76	6.73±1.03	9.71±1.64	10.86±2.58
CPOL	2.80±0.41	2.76±0.52	2.93±0.66	3.57±0.95
MCPR	2.24±0.35	2.28±0.37	2.34±0.59	2.53±0.62

Fig. 13. Average multi-scale complex phase order representation across all scales for a real-world ultrasound image of the prostate.

well captured using the proposed approach despite the high speckle noise level, thus illustrating the noise robustness of the proposed approach.

IX. CONCLUSIONS

In this work, a Bayesian theoretic approach to multi-scale complex phase order representations was explored. Experimental results illustrate the approach's potential for constructing multi-scale complex phase order representations that exhibit strong structural localization and noise resilience, as well as the effectiveness of the constructed multi-scale representations for computer vision tasks such as multimodal image registration. Future work involves investigating the proposed approach for other image processing tasks such image reconstruction and restoration, as well as other computer vision tasks such as salient feature detection.

ACKNOWLEDGMENT

REFERENCES

[1] M. Morrone and R. Owens, "Feature detection from local energy," *Pattern Recognition Letters*, vol. 6, pp. 303–313, 1987.
[2] M. Morrone and D. Burr, "Feature detection in human vision: A phase-dependent energy model," *Proceedings of Royal Society of London B*, vol. 235, pp. 221–245, 1988.
[3] M. Thomson, "Visual coding and the phase structure of natural scenes," *Network: Computation in Neural Systems*, vol. 10, pp. 123–132, 1999.
[4] P. Kovesi, "Phase congruency: A low-level image invariant," *Psychological Research*, vol. 64, no. 2, pp. 136–148, 2000.
[5] Y. Tian, "Autofocus using image phase congruency," *Optical Express*, vol. 19, pp. 261–270, 2011.
[6] Z. Wang and E. Simoncelli, "Local phase coherence and the perception of blur," in *Advances in Neural Information Processing Systems*, pp. 1435–1442, 2004.
[7] S. Gundimada and K. Asari, "A novel feature selection strategy on fused thermal and visible cameras for improved face recognition in the presence of extreme lighting and facial variations," in *Face Biometrics for Personal Identification: Multi Sensory Multi-Modal Systems, Signals and Communication Technology Series*, pp. 109–120, 2008.
[8] L. Qing, S. Shan, X. Chen, and W. Gao, "Face recognition under varying lighting based on the probabilistic model of gabor phase," in *Proceedings of International Conference on Pattern Recognition*, pp. 1139–1142, 2006.
[9] A. Wong, "Illumination invariant active contour-based segmentation using complex-valued wavelets," in *Proceedings of IEEE International Conference on Image Processing*, 2008.
[10] A. Belaid, D. Boukerroui, Y. Maingourd, and J. Lerallut, "Phase based level set segmentation of ultrasound images," in *Proceedings of International Conference on Information Technology and Applications in Biomedicine*, pp. 1–4, 2009.
[11] I. Hacihaliloglu, R. Abugharbieh, A. Hodgson, and R. Rohling, "Bone segmentation and fracture detection in ultrasound using 3d local phase features," in *Proceedings of Med Image Comput Comput Assist Interv.*, pp. 287–295, 2008.
[12] A. Wong, D. A. Clausi, and P. Fieguth, "CPOL: Complex phase order likelihood as a similarity measure for mr-ct registration," *Medical Image Analysis*, vol. 14, no. 1, pp. 50–57, 2010.
[13] O. Sadowski, Z. Yaniv, and L. Joskowicz, "Comparative in-vitro study of contact and image-based rigid registration for computer-aided surgery," *Computer-Aided Surgery*, vol. 7, no. 4.
[14] V. Walimbe, O. Dandekar, F. Mahmoud, and R. Shekhar, "Automated 3d elastic registration for improving tumor localization in whole-body pet-ct from combined scanner," in *Proceedings of the Annual International Conference of the IEEE Engineering in Medicine and Biology Society*, pp. 2799–2802, 2006.
[15] S. Viswanath, J. Chappelow, P. Patel, B. Bloch, N. Rofsky, R. Lenkinski, E. Genega, and A. Madabhushi, "Enhanced multi-protocol analysis via intelligent supervised embedding (empravise): detecting prostate cancer on multi-parametric mri," in *Proceedings of SPIE Medical Imaging*, 2011.
[16] D. Langer, T. van der Kwast, A. Evans, J. Trachtenberg, B. Wilson, and M. Haider, "Prostate cancer detection with multi-parametric mri: Logistic regression analysis of quantitative t2, diffusion-weighted imaging, and dynamic contrast-enhanced mri," *Journal of Magnetic Resonance Imaging*, vol. 30, no. 2, pp. 327–334, 2009.
[17] I. Selesnick, W. Ivan, R. Baraniuk, and N. Kingsbury, "The dual-tree complex wavelet transform," *IEEE Signal Processing Magazine*, vol. 22, no. 6, pp. 123–151, 2005.
[18] S. Fischer, F. Sroubek, L. Perrinet, R. Redondo, and G. Cristoba, "Self-invertible 2d log-gabor wavelets," *International Journal of Computer Vision*, vol. 75, no. 2, pp. 231–246, 2007.
[19] T. Lindeberg, "Scale-space: A framework for handling image structures at multiple scales," in *Proceedings of CERN School of Computing, Egmond aan Zee, The Netherlands*, 1996.
[20] A. Witkin, "Scale-space filtering," in *7th International Joint Conference on Artificial Intelligence*, pp. 1019–1022, 1983.
[21] J. Koenderink and A. V. Doorn, "The structure of images," *Biological Cybernetics*, pp. 363–370, 1984.
[22] A. Hummel, "Representations based on zero-crossings in scale space," in *Proceedings of the IEEE Computer Vision and Pattern Recognition Conference*, pp. 204–209, 1986.
[23] J. Babaud, A. Witkin, M. Baudin, and R. Duda, "Uniqueness of the gaussian kernel for scale-space filtering," *IEEE Transactions on Pattern Analysis and Machine Intelligence*, vol. PAMI-8, 1986.
[24] T. Lindeberg, "Scale-space for discrete signals," *IEEE Transactions on Pattern Analysis and Machine Intelligence*, vol. PAMI-12, no. 3, pp. 234–254, 1990.

14

[25] P. Perona and J. Malik, "Scale-space and edge detection using anisotropic diffusion," *IEEE Transactions on Pattern Analysis and Machine Intelligence*, vol. 12, no. 7, pp. 629–639, 1990.

[26] R. Whitaker and S. Pizer, "A multi-scale approach to nonuniform diffusion," *Computer Vision, Graphics, and Image Processing*, vol. 57, no. 1, pp. 99–9660, 1993.

[27] L. Florack, A. Salden, B. ter Haar Romeny, J. Koenderink, and M. Viergever, "Nonlinear scale-space," *Image and Vision Computing*, vol. 13, no. 4, pp. 279–294, 1995.

[28] J. Weickert and B. Benhamouda, "A semidiscrete nonlinear scale-space theory and its relation to the perona-malik paradox," *Advances in computer vision*, pp. 1–10, 1997.

[29] A. Salden, "Bluman and kumei's nonlinear scale-space theory." Technical Report, February 1999.

[30] P. Fieguth, *Statistical Image Processing and Multidimensional Modeling*. Springer, 2010.

[31] P. Davis and P. Rabinowitz, *Methods of Numerical Integration*. Dover Publications, 2007.

[32] Z. Wang, A. C. Bovik, H. R. Sheikh, and E. P. Simoncelli, "Image quality assessment: From error visibility to structural similarity," *IEEE Transactions on Image Processing*, vol. 13, no. 4, pp. 600–612, 2004.

[33] S. Geman and D. McClure, "Statistical methods for tomographic image reconstruction," *Bulletin of the International Statistical Institute*, vol. LII-4, pp. 5–21, 1987.

[34] K. Johnson and J. Becker, "The whole brain atlas." World Wide Web Document, February 2009. http://www.med.harvard.edu/AANLIB/home.html.

[35] P. Boggs and J. Tolle, "Sequential quadratic programming," *Acta Numerica*, pp. 1–51, 1995.

[36] C. Studholme, D. Hill, and D. Hawkes, "An overlap invariant entropy measure of 3d medical image alignment," *Pattern Recognition*, vol. 32, no. 1, pp. 71–86, 1999.

[37] M. Mellor and M. Brady, "Phase mutual information as a similarity measure for registration," *Medical Image Analysis*, vol. 9, pp. 330–343, 2005.

[38] G. Cao, P. Shi, and B. Hu, "Ultrasonic liver discrimination using 2-d phase congruency," *IEEE Transactions on Biomedical Engineering*, vol. 53, no. 10, pp. 2116–2119, 2006.
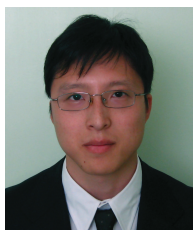
Alexander Wong (M '05) received the B.Sc. degree in computer engineering, the M.Sc. degree in electrical and computer engineering, and the Ph.D. degree in Systems Design Engineering in 2005, 2007, and 2010, respectively, from the University of Waterloo, Waterloo, ON, Canada. He was a postdoctoral fellow from 2010 to 2011 at Sunnybrook Hospital and the University of Toronto, Toronto, ON. He is currently an assistant professor in the Department of Systems Design Engineering at the University of Waterloo. He is also with the Vision and Image Processing Research Group, University of Waterloo. He has authored or coauthored papers in various fields such as computer vision, graphics, image processing, biomedical signal processing, and multimedia systems, published in refereed journals and conferences. His current research interests include biomedical image processing and analysis, remote sensing, computer vision, and pattern recognition.